Stability of reduced $V_2O_5(001)$ surfaces

M. V. Ganduglia-Pirovano* and J. Sauer
Humboldt Universität zu Berlin, Institut für Chemie, Arbeitsgruppe Quantenchemie, Unter den Linden 6, D-10099 Berlin, Germany
(Received 3 February 2004; revised manuscript received 19 March 2004; published 29 July 2004; corrected 9 November 2004)

The defect-free $V_2O_5(001)$ surface and ordered structures involving oxygen vacancies have been studied for a wide range of defect concentrations, Θ ($1/6 \leqslant \Theta \leqslant 1$ monolayer, ML), combining density functional theory and statistical thermodynamics. At $\Theta = 1/4$ ML the oxygen vacancy formation energy for the singly coordinated surface oxygen atoms (vanadyl oxygen, O^1) is by ~1.7 eV/atom and ~2.0 eV/atom lower than the corresponding values for two- and threefold coordinated surface oxygen atoms, respectively. Between 1/3 and 1/2 ML the alignment of vanadyl oxygen vacancies (O^1_{vac}) along the [010] direction is by 70 meV/atom ($\Theta = 1/3$ ML) and 120 meV/atom ($\Theta = 1/2$ ML) more favorable than along the [100] direction, with the concentration-induced change of the vacancy formation energy for structures with vacancies aligned along the [100] direction being smaller than 20 meV/atom. The lowest vacancy formation energy of 1.87 eV/atom corresponds to the (1×1)-O^1_{vac} ($\Theta = 1/2$ ML) phase with defects forming a trenchlike structure with rows along the [010] direction. Above 1/2 ML the vacancy formation energy increases up to 2.07 eV/atom ($\Theta = 1$ ML). The ease of formation of nonrandom vacancy structures with a favored alignment along the [010] direction is discussed in terms of special vacancy-induced lattice distortions. It is also argued that the trenches along the [010] direction provide preferred paths for continuous reduction of the surface starting from isolated defect sites. However, this missing-row structure would be stable only at very low oxygen partial pressures close to conditions for which V_2O_5 decomposes into VO_2 and O_2.

DOI: 10.1103/PhysRevB.70.045422 PACS number(s): 68.47.Gh, 68.35.Md, 68.35.Bs, 68.35.Dv

I. INTRODUCTION

Vanadium oxides are widely used in the manufacture of important chemicals and in the reduction of environmental pollution. In fact, all the heterogeneous oxide catalysts used on industrial scale for production of organic anhydrides and acids contain vanadium as the main component of the active phase.[1] The catalytic behavior of vanadia in several oxidation reactions has been discussed based on the Mars and van Krevelen mechanism,[2] in which the reactant molecule is oxidized by the catalyst, which is then oxidized by gas-phase oxygen. Yet, the origin of the oxygen which is incorporated into a hydrocarbon molecule is a matter of debate. Regardless of this open question, in the stationary state of the oxidation reaction all catalysts contain vanadium with a variety of oxidation states (i.e., V^{+5}, V^{+4}, and V^{+3}) and coordination environments (see Ref. 1 and references therein), and many suggested reaction mechanisms include the removal of oxygen from the catalyst as a critical step. Thus, the ease of removal of oxygen from the lattice of V_2O_5 is of particular interest and an important factor allowing this oxide to function as catalyst in selective oxidation.

In this article we report periodic density functional theory (DFT) calculations for oxygen vacancies at the $V_2O_5(001)$ surface. Special attention will be paid to the dependence of the average vacancy formation energy on the vacancy concentration and the vacancy-induced changes of the geometric and electronic structures. The stability of the partially reduced $V_2O_5(001)$ surface at finite temperatures will be discussed as a function of the oxygen partial pressure in the gas phase. V_2O_5 has a layer-type structure and orthorhombic symmetry.[3] The (001) plane is the easy cleavage plane. In bulk V_2O_5 there are three structurally different oxygen atoms in each layer: vanadyl oxygen, O^1, coordinated to one vanadium atom, bridging oxygen atoms, O^2, and two threefold coordinated oxygen atoms, O^3 and $O^{3'}$, respectively (cf. Fig. 1). So far, only a few theoretical studies have been devoted to oxygen vacancies at the $V_2O_5(001)$ surface. Lambrecht *et al.* have only investigated the electronic structure of surface vanadyl oxygen vacancies using a periodic single-layer tight-binding model of the surface with frozen geometry,[4] and argued[5] that relaxations which introduce new types of inter-

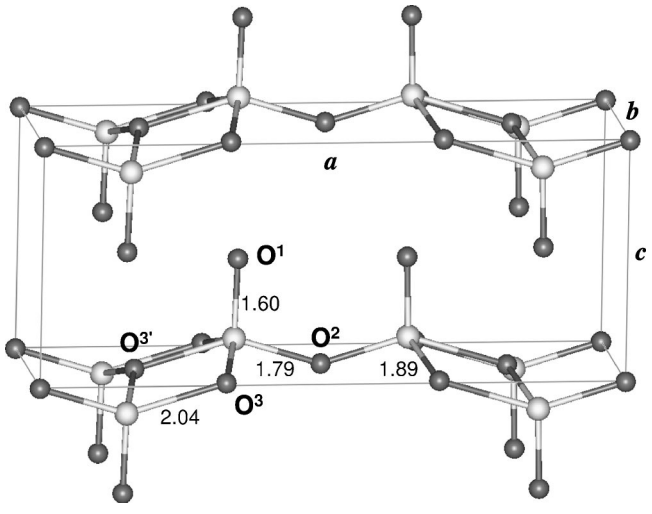

FIG. 1. V_2O_5 bulk structure. V atoms are depicted as the white circles and the O atoms as the smaller gray circles. O^1 and O^2 denote the single and twofold coordinated oxygen atoms, respectively. O^3 and O^3 are two threefold coordinated lattice oxygen atoms. Bond lengths in Å.

layer coupling are not to be expected. Hermann *et al.* performed DFT calculations using the RPBE (revised Perdew-Burke-Ernzerhof) functional[6] on oxygen vacancies at the $V_2O_5(001)$ surface using cluster models.[7] They found that the calculated vanadyl oxygen vacancy formation energy decreases by about 1.0 eV/atom when increasing the size of the clusters from one to two crystal layers. This difference is due to oxygen vacancy-induced lattice relaxations that affect the interlayer binding.

It is known that V_2O_5 is easily reduced by low-energy particle bombardment,[8–11] and it is frequently claimed that the vanadyl oxygen is the one playing the most important role in catalytic oxidation reactions. However, there is no experimental proof. The theoretical investigations of Ref. 7 and the present calculations have asserted that the vacancy formation energy of isolated singly coordinated surface oxygen atoms is lowest among the five structurally nonequivalent oxygen atoms at the $V_2O_5(001)$ surface.

The experimental characterization of the reduced $V_2O_5(001)$ surface is possible with modern surface science methods such as scanning tunneling microscopy (STM), but recent applications to this system are still missing. Images of the $V_2O_5(001)$ surface cleaved in ultrahigh vacuum (UHV) and at room temperature were recorded and inhomogeneities in the surface observed.[12] The vanadyl O is easily removed from the surface as a result of the cleavage, and vacancies are left behind in a *nonrandom* distribution. Therefore, in this work, we determine the stability of reduced $V_2O_5(001)$ surfaces for different perfectly ordered structures with varying vanadyl oxygen vacancy concentration. It is possible that disordered or even incommensurate structures might lead to a lower energy.

The remainder of this paper is organized as follows: The calculation method is briefly explained in Sec. II, and in Sec. III zero temperature and zero pressure results are presented for the defect-free $V_2O_5(001)$ surface and structures involving oxygen vacancies. Energies, structures, and electronic properties are described for a wide range of defect concentrations. In Sec. IV we present the calculated surface free energies of structures with oxygen deficiencies in thermodynamic equilibrium with an environment of defined oxygen partial pressure at finite temperature and discuss their stability. In Sec. V our results are summarized.

II. COMPUTATIONAL DETAILS AND MODELS

Calculations are based on spin-density functional theory (DFT) (Refs. 13 and 14) and employ a plane-wave basis set[15] as implemented in the Vienna *ab initio* simulation package (VASP).[16–19] We use the exchange-correlation functional of Perdew *et al.* (PW91).[20,21] The electron-core interaction is described by the projector augmented wave (PAW) method as proposed by Blöchl.[22] Compared to conventional pseudopotentials, this method has the advantage that the exact shape of the valence wave function is taken into account, and this in turn can improve the description of transition metals.[23] A core radius of 1.2 Å is used for V. The 3*p* states of V are treated as valence states to guarantee a good transferability of the V potential. For oxygen, core radii of 0.6 and 0.8 Å are used for the *s* and *p* states, respectively. All calculations are performed at an energy cutoff of 800 eV.

The $V_2O_5(001)$ surface is modeled using the supercell approach, where we use a two-layer (001) oriented slab with a vacuum region corresponding to two interlayer spacings ($\sim$10 Å). In the defect-free surface case, two equivalent surfaces are created. The structures involving oxygen vacancies have been studied for a wide range of defect concentrations Θ. We have considered $\Theta = 1/6$, $1/4$, $1/3$, $1/2$, $3/4$, and 1.0 ML with a (1×3), (1×2), and (1×1) surface periodicity. In total, 10 structures have been investigated. The vacancies are created by removing surface oxygen atoms from one of the layers only, so that partially reduced slabs without the same surface termination on top and at the bottom are formed.

The Brillouin-zone (BZ) sampling is based on the Monkhorst-Pack technique.[24] A $(2\times6\times1)$ grid has been used for the (1×1) primitive surface unit cell. These are 12 *k* points that do not include the $\bar{\Gamma}$ point. For the (1×3) and (1×2) surface unit cells, grids have been chosen so as to obtain the same sampling of the reciprocal space [$(2\times2\times1)$-, and $(2\times3\times1)$ meshes, respectively], and thus maintain the same accuracy when comparing the vacancy formation energies at different defect concentrations. The relaxation of the ionic positions into the ground state is performed within a quasi-Newton scheme. All atoms are allowed to relax. In Sec. III the accuracy of the numerical approximations made with the present computational setup is judged on selected calculations performed using a thicker slab (three layers), a denser *k*-point grid, and a higher cutoff.

III. RESULTS AND DISCUSSION

A. Bulk and $V_2O_5(001)$ surface structure

To determine oxygen vacancy-induced effects on the $V_2O_5(001)$ surface structure, we first investigated the defect-free surface. The surface cell was set up with the calculated bulk lattice parameters. The unit cell contains 14 atoms (2 formula units).[3] Cell-shape minimizations that included the simultaneous optimization of the fractional coordinates have been performed for several fixed volumes, and the equilibrium volume has been obtained by fitting to the Murnaghan equation of state.[25] After an additional minimization of the cell shape and fractional coordinates at the calculated equilibrium volume the values $a = 11.550$ Å, $b = 3.576$ Å, and $c = 4.836$ Å have been obtained. In Table I, these values are compared with the corresponding experimental values[3] and with those obtained in other theoretical studies.[26–30]

The deviations $\Delta a/a$, $\Delta b/b$, and $\Delta c/c$ of the PW91 calculated lattice parameters a, b, and c from the experimentally observed values are approximately 2%, 1%, and 11%, respectively. The interaction between the V_2O_5 crystal layers is of van der Waals type. Present DFT methods do not properly account for these weak interactions[31,32] resulting in an extremely flat potential energy surface, and this explains the larger deviations in the calculated *c*-lattice parameter. Similar results have been obtained for the interlayer binding in

TABLE I. Calculated lattice parameters in Å for bulk V_2O_5. The experimental data are from Ref. 3. Results are compared with those of other calculations using the same gradient corrected approximation (PW91) but other potentials (Refs. 26–29) (see the corresponding references for details). In Ref. 30 the local-density approximation and the all-electron full-potential linear muffin-tin method have been employed.

	a	*b*	*c*
Expt.[a]	11.51	3.56	4.37
This work	11.55	3.58	4.84
PW91/Lee-PP[b]	11.53	3.60	4.42
PW91/US-PP[c]	11.70	3.59	4.47
PW91/PAW[d]	11.65	3.57	4.69
PW91/TM-PP[e]	11.62	3.59	4.44
LDA/FP-LAPW[f]	11.38	3.52	4.32

[a]Reference 3.
[b]Reference 26.
[c]Reference 27.
[d]Reference 28.
[e]Reference 29.
[f]Reference 30.

MoS_2[33] and in graphite.[34] The computed V-O bond distances (see Fig. 1 and Table II) $d_{V-O^1}=1.60$ Å, $d_{V-O^2}=1.79$ Å, $d_{V-O^3}=1.89$, and $d_{V-O^{3'}}=2.04$ Å compare well with the corresponding experimental values of 1.58, 1.78, 1.88, and 2.02 Å, respectively, and are in line with other DFT-GGA results.[26,29] For this calculation we used a $(2\times4\times4)$-*k* mesh and an energy cutoff of 800 eV. The calculated bulk lattice parameters change by less than 0.02% if a $(2\times6\times6)$-*k* mesh is used. The latter corresponds to the $(2\times6\times1)$ mesh used for the (1×1) surface cells. As already indicated in Sec. II, this grid choice guarantees the same sampling of the reciprocal space for the larger surface unit cells considered, namely (1×2) and (1×3). The changes induced by a cutoff increase up to 1200 eV are of the same order of magnitude (less than 0.02%).

The V_2O_5 surface relaxations are small. The outermost d_{V-O^1} distances are shorter by less than 0.01 Å, d_{V-O^2} distances are larger by approximately the same amount, and among the d_{V-O^3} distances changes are not larger (see Table II). The above-mentioned weak interactions between the layers result in small, surface-induced relaxations upon cleavage of the bulk structure to create the (001) oriented surface. The calculated surface energies are 0.040 J/m^2 for the relaxed surface and 0.048 J/m^2 for the bulk-truncated surface geometry. The former value is converged with respect to slab and vacuum thicknesses. Corresponding calculations for a two-layer (three-layer) slab with a vacuum thickness corresponding to three (two) interlayer spacings change the surface energy by less than ±0.001 J/m^2. These calculations were performed using the same *k* mesh and cutoff as for the optimization of the bulk lattice geometry. In the following, unless indicated, a two-layer slab with a vacuum thickness corresponding to two interlayer spacings is used.

TABLE II. Calculated V-O bond distances in Å for the bulk V_2O_5 structure and its (001) oriented surface. For the surface structure, d_{V-O^1} corresponds to the vanadyl bonds sticking out of the surface, and for the other distances an average bond length between similar bonds in both substrate layers is given (d_{V-O^i}, $i=2$, 3, and 3′).

	Bulk (Expt.[a])	Bulk	V_2O_5(001)
d_{V-O^1}	1.58	1.60	1.59
d_{V-O^2}	1.78	1.79	1.80
d_{V-O^3}	1.88	1.89	1.90
$d_{V-O^{3'}}$	2.02	2.04	2.05

[a]Reference 3.

The very small surface energy correlates with the known weak nature of the interlayer bonding. The (001) plane is the easy cleavage plane. Atomically clean (001) surfaces are easily obtained by either pushing a razor blade into the crystal[11] or by pulling off very thin layers using Scotch tape.[35]

B. O-vacancy-induced surface relaxations

The presence of vanadyl oxygen vacancies on a V_2O_5(001) surface was investigated at six different concentrations $\Theta=1/6$, $1/4$, $1/3$, $1/2$, $3/4$, and 1.0 ML. At $\Theta=1/3$ and $1/2$ concentrations, different patterns with vacancies sharing either none, a two-, or a threefold coordinated surface oxygen atom were studied. Figure 2 shows the considered structures.

The calculated average vacancy formation energies as a function of vacancy concentration are discussed in the next section (III C). To provide a framework for the understanding of these energies, in this section we characterize the geometrical structures of these reduced surfaces and examine the vacancy-induced relaxations. First, we discuss the significant changes at the lowest surface O-vacancy concentration ($\Theta=1/6$ ML). Figure 3 shows that removal of $1/6$ of the surface vanadyl O atoms results in noticeable changes in the immediate vicinity of the surface vacancy site, V_{vac}, and a considerable distortion of the interlayer spacing. Namely, at the defect sites (V_{vac}) vanadium atoms relax inwards while the vanadyl group right below the defect site relaxes in the opposite direction resulting in a local contraction and the formation of a *real* bond between the layers. The resulting V-O bond lengths [1.78 and 1.77 Å, Fig. 3(b)] are longer by $\sim$11% than the bond length between vanadyl oxygen and V in bulk V_2O_5 (1.60 Å). Moreover, the V-O^2-V angle changes from $\sim$151° in the defect-free surface [Fig. 3(a)] to $\sim$178° for the V-O^2-V_{vac} [Fig. 3(b)]. The corresponding V-O^2 bonds change from 1.80 Å to 1.88 and 1.72 Å. Structural distortions are also observed for the V-O^2-V angle and the corresponding V-O^2 bonds in the second layer right below such stretched V-O^2-V_{vac} angle in the surface layer. The local environment of the V_{vac} site is shown in the insert of Fig. 3(b). All four V_{vac}-O bonds within the surface layer are shorter by up to $\sim$0.1 Å compared to the defect-free V_2O_5(001) surface. Similar bond length changes are observed for the corresponding bonds of the V atom right below V_{vac} in the second layer.

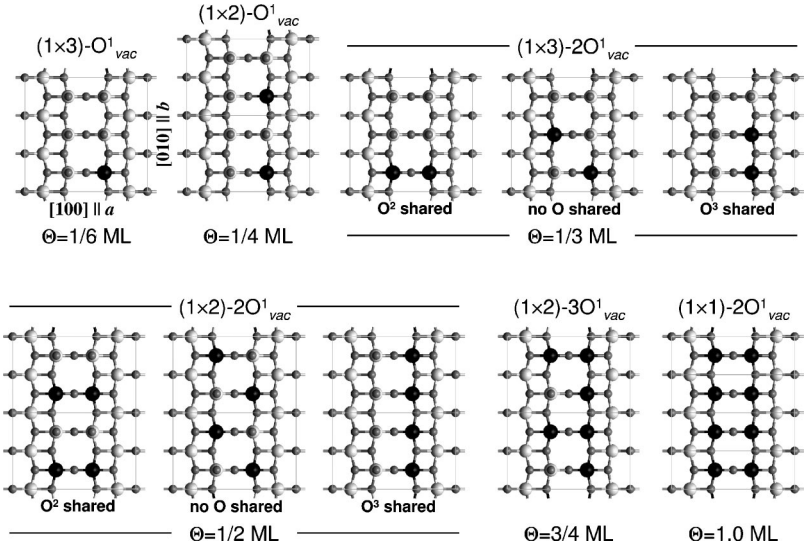

FIG. 2. Schematic top view of all superstructures investigated as a function of the surface vanadyl oxygen concentration Θ in monolayers (ML). The various V sites at the surface that are depicted as black circles correspond to the O^1_{vac} vacancy site and the white and gray circles represent V and O atoms, respectively.

Increasing the defect concentration leads to additional lattice deformations that are different depending on the location of the neighboring vacancy. As mentioned above, different geometrical arrangements exist at total concentrations of 1/3 and 1/2 ML (see Fig. 2). If vacancies share O^3 atoms, pairs (rows) of defects along the [010] direction can be formed at Θ=1/3 ML (Θ=1/2 ML), respectively. In case only O^2 atoms are shared, vacancies are aligned along the [100] direction, forming structures with different periodicity, namely (1×3) and (1×2) at Θ=1/3 and 1/2 ML, respectively. To discuss the effect of these two different vacancy orderings (V_{vac}-O^i-O_{vac}, $i=2,3$) in the overall surface structure, we consider next the two (1×3)-$2O^1_{vac}$ structures at Θ=1/3 ML with defect pairs along the [010] (O^3 shared) and [100] (O^2 shared) directions and compare them with isolated vacancies at Θ=1/6 ML.

Figures 4(a) and 4(b) display the fully relaxed local environment induced by vacancy pairs that share either an O^3 or O^2 atom, respectively. For the former the atomic displacements around each vacancy are of the same order of magnitude as those for an isolated vacancy at 1/6 ML [cf. Fig. 3(b)]. Both V-O^2-V_{vac} angles equal 176° and values of 147°

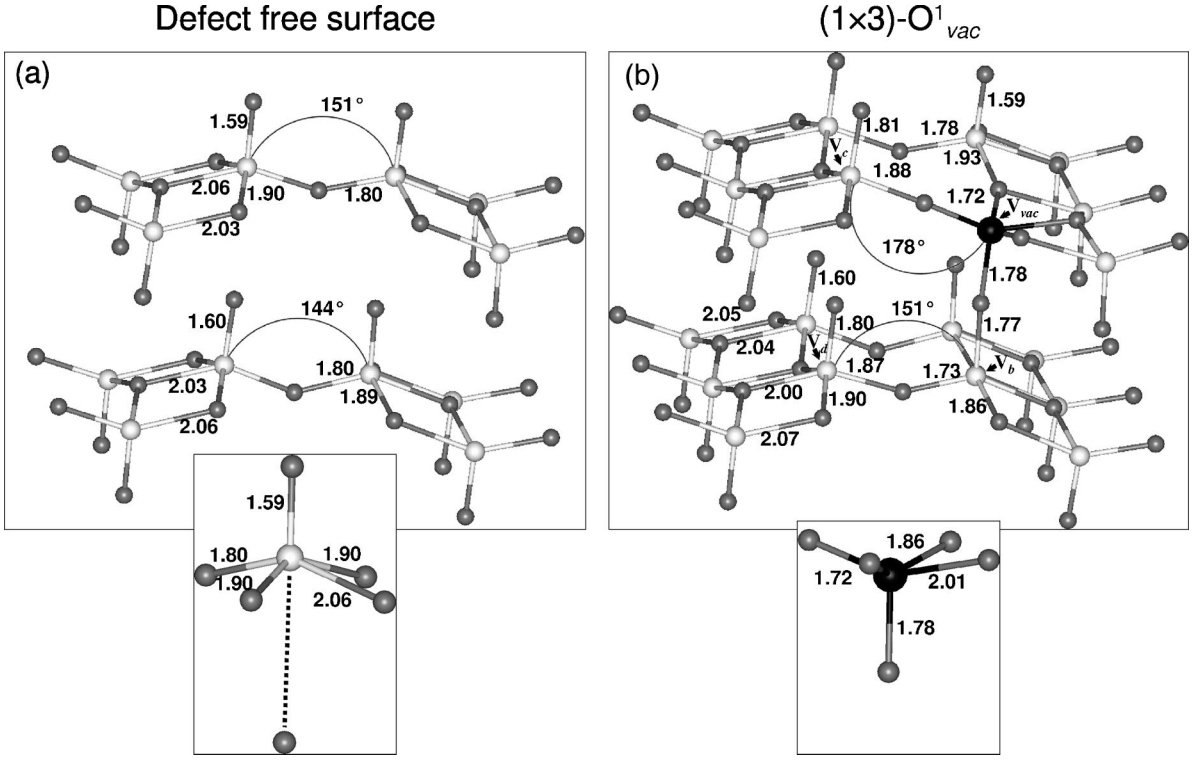

FIG. 3. Atomic geometry of (a) the defect-free V_2O_5(001) surface, and (b) a selected region of the optimized (1×3)-O^1_{vac} structure (Θ=1/6 ML). The vacancy site at the surface is depicted as the black circle, V atoms as the white circles, and the O atoms as the smaller gray circles. Selected bond lengths in Å.

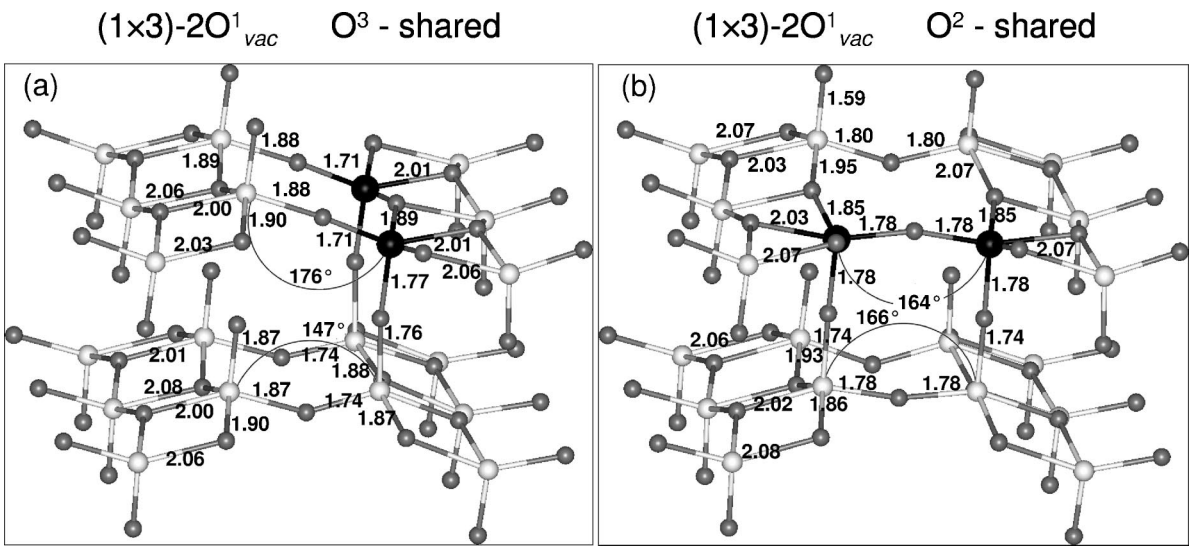

FIG. 4. Atomic geometry of selected regions of optimized structures at $\Theta = 1/3$ ML: (a) (1×3)-$2O^1_{vac}$ with vacancies sharing a threefold coordinated surface oxygen atom; (b) as for (a) but vacancies share a twofold coordinated oxygen atom. The various vacancy sites at the surface are depicted as black circles, V atoms as white circles, and the O atoms as smaller gray circles. Selected bond lengths in Å.

are calculated for the corresponding V-O^2-V angles in the second layer. Furthermore, comparison of Fig. 3(b) and Fig. 4(a) reveals that the additional vacancy, that shares a threefold coordinated atom with the first one and forms a [010] oriented pair, induces small changes in the local geometry of the already existing defect. In other words, the magnitude of the changes in bond lengths between the atoms included in a volume which corresponds to 1/3 of the total unit cell volume that includes the first vacancy is not larger than 0.03 Å *after* the pair formation. Thus, noncounteracting vacancy-induced relaxation effects with increasing coverage (from 1/6 to 1/3 ML) are observed when vacancies align along the [010] direction.

Turning to defects that share a twofold coordinated oxygen atom at $\Theta = 1/3$ ML and form [100] oriented pairs [see Fig. 4(b)], we find the above mentioned downward relaxation of surface V_{vac} atoms and the corresponding upward relaxation of the V atoms of the second layer so that a square-*like* structure is formed. The V_{vac}-O^2-V_{vac} and V-O^2-V angles are 164° and 166° in the surface and second layer, respectively. The V-O^2-V angles in the next (010) plane (without defects) do not seem to be affected by the presence of the vacancies. They differ by a mere ~1° from the corresponding values for the defect-free surface.

In contrast to [010] oriented vacancy pairs, the lattice relaxations induced by additional vacancies (that form [100] oriented pairs) do *not* appear to take place cooperatively. As discussed above, the geometry originated from 1/6 ML shows a stretched V-O^2-V_{vac} angle in the surface layer and the corresponding V-O^2 bonds are elongated or shortened by approximately 0.1 Å when compared to the defect-free surface (cf. Fig. 3). Similar bond lengths changes are found in the second layer. The additional vacancy forming a [100] oriented pair at 1/3 ML [cf. Fig. 4(b)] brings the V-O^2-V angles and the corresponding bonds *back* to a more symmetric configuration; the lattice relaxations resulting from an isolated defect are counteracted by those induced by the subsequent vacancy when vacancies align along the [100] direction.

Similar considerations apply when the concentration is further increased from 1/3 to 1/2 ML and structures are allowed to relax with vacancies sharing either O^2 or O^3 atoms. For the former case, increasing Θ up to 1/2 ML does not induce a sizable effect in the local environment of vacancy sites already present at 1/3 ML. This is not surprising since, by increasing the concentration from 1/3 to 1/2 ML, the distance between vacancies along the [010] direction has decreased by ~3.6 Å, but it is still as large as ~7.2 Å (i.e., twice the *b*-lattice parameter). Therefore, the average vacancy formation energy for these structures is likely to be pretty similar (see Sec. III C).

When vacancies share O^3 atoms and the concentration increases from 1/3 to 1/2 ML, a trench-like structure with a (1×1) periodicity and vacancy rows along the [010] direction forms (cf. Fig. 2). Similar to what was found for a concentration increase from 1/6 to 1/3 ML, the lattice relaxations seem to take place in a consecutive way with no counteractive effect. That is, the additional vacancies that lead to the row formation do not sizably affect the local environment of the existing vacancy pairs, and it is possible that the incipient trench induced by the [010] oriented pairs facilitates the occupation of additional sites along the trench. This discussion will be relevant when considering the average vacancy formation energy of these structures (see Sec. III C) and in turn the stability of the reduced surfaces as a function of the oxygen partial pressure in the gas phase (see Sec. IV).

C. O-vacancy formation energy

The average vacancy formation energy as a function of vacancy concentration $\Theta = N_{vac}/N_{tot}$ is given by

TABLE III. Averaged surface vanadyl vacancy formation energy $E_f^{(1/2)O_2}$ in eV/atom for the unrelaxed and relaxed structures investigated.

Θ [ML]	Structure	Unrelaxed	Relaxed
1/6	(1×3)-O^1_{vac}	3.76	1.93[a]
1/4	(1×2)-O^1_{vac}	3.78	1.95
1/3	(1×3)-$2O^1_{vac}$ (O^3 shared)	3.77	1.90
	(1×3)-$2O^1_{vac}$ (no O shared)	3.77	1.95
	(1×3)-$2O^1_{vac}$ (O^2 shared)	3.74	1.97
1/2	(1×2)-$2O^1_{vac}$ (O^3 shared)	3.79	1.87
	(1×2)-$2O^1_{vac}$ (no O shared)	3.80	1.96
	(1×2)-$2O^1_{vac}$ (O^2 shared)	3.76	1.99
3/4	(1×2)-$3O^1_{vac}$	3.80	1.99
1.0	(1×1)-$2O^1_{vac}$	3.83	2.07

[a]Reference 56.

$$E_f^{O}(\Theta) = \frac{1}{N_{vac}}[E_{vac}(\Theta) - E_{clean} + N_{vac}E_O], \quad (1)$$

where N_{vac} and N_{tot} are the actual and maximum number of vacancies in the unit cell, $E_{vac}(\Theta)$, E_{clean}, and E_O represent the total energies of the reduced surface slab, the defect-free surface slab, and the free oxygen atom, respectively. In the following, $E_f^{(1/2)O_2}$ indicates the use of the molecular reference energy in Eq. (1), i.e.,

$$E_f^{(1/2)O_2}(\Theta) = \frac{1}{N_{vac}}\left[E_{vac}(\Theta) - E_{clean} + N_{vac}\frac{1}{2}E_{O_2}\right]. \quad (2)$$

A positive number for $E_f^{(1/2)O_2}$ indicates that the vacancy formation is endothermic and the difference between E_f^O and $E_f^{(1/2)O_2}$ is just half the dissociation energy of the O_2 molecule.

The total energies of the isolated O atom and the O_2 molecule, which are involved in the calculation of E_f^O and $E_f^{(1/2)O_2}$, respectively, have been calculated in a tetragonal cell of side lengths $a=10$ Å, $b=11$ Å, and $c=12$ Å with Γ-point sampling of the Brillouin zone (other parameters as in Sec. II). The binding energy per O atom in O_2 is calculated to be 3.13 eV/atom and the bond distance 1.234 Å. The experimental results are 2.59 eV/atom (obtained after adding the contributions due to zero-point vibrations to the $T=0$ K value) and 1.207 Å, respectively.[36] The overestimation of the binding energy and the bond distance are in line with earlier density functional calculations that used gradient corrected functionals.[37,38]

Table III and Fig. 5 summarize the calculated average O-vacancy formation energies at the $V_2O_5(001)$ surface for the superstructures investigated. Table III shows that $E_f^{(1/2)O_2}$ does not depend strongly on the vacancy concentration. However, the lattice relaxations described in the previous section have a large effect on the vacancy formation energy. For the unrelaxed structures the vacancy formation energy is about ~2 eV/atom higher than for the fully relaxed structures (cf. Table III and Fig. 5). The largest lattice relaxation effect is the formation of a bond between the layers at each defect site. The relaxation contributions to the vacancy formation energy are very similar for all defect structures investigated. Note, however, that vacancies sharing threefold coordinated O atoms have larger relaxation contributions than vacancies sharing twofold coordinated O atoms.

The vacancy formation energy at $\Theta=1/6$ ML represents the isolated vacancy limit. Increasing the concentration up to 1/4 ML increases the energy by 20 meV/atom only. This is not surprising since the vacancies at $\Theta=1/4$ ML are still separated by four V-O^3 bonds (~7.2 Å). Gradually increasing the concentration from 1/4 ML to 1/3 and 1/2 ML leads to somewhat larger effects and similar trends for both steps (see Fig. 5). While the vacancy formation energy increases by up to ~40 meV/atom with vacancies sharing only twofold coordinated oxygen atoms, the (1×3) and (1×2) phases with defects sharing threefold coordinated oxygen atoms are, respectively, by 50 and 80 meV/atom energetically favored (relative to $\Theta=1/4$ ML). Each vacancy site is virtually not influenced by the others if vacancies do not share oxygen atoms at 1/3 and 1/2 ML, respectively.

To test the accuracy of our calculated vacancy formation energies on a number of numerical approximations, namely the cutoff energy of the plane-waves basis set, the number of

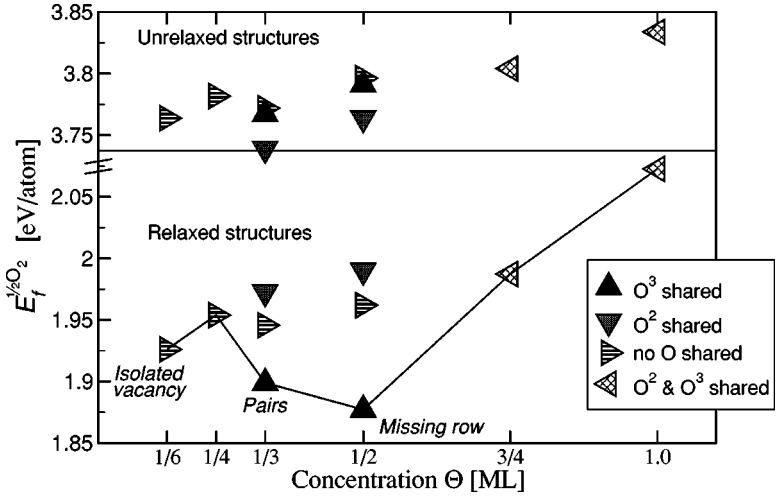

FIG. 5. Calculated average vacancy formation energies $E_f^{(1/2)O_2}$ in eV/atom as a function of the vacancy concentration Θ on $V_2O_5(001)$ for the unrelaxed (top panel) and relaxed (lower panel) surface structures investigated. The right, down, and up oriented triangles correspond to structures in which vacancies do not share, only share O^3 or O^2 surface oxygen atoms, respectively. The structures in which both type of O atoms are shared are indicated by left-oriented triangles and the lowest energy structures at each concentration are connected by a line.

k points and the slab thickness, selected calculations were repeated with more accuracy. A $(2\times6\times1)$ *k* mesh for the (1×1) surface unit cell, a two-layers slab (with ~10 Å vacuum), and 800 eV correspond to the standard setup (cf. Sec. II). We calculated the average vacancy formation energy at the highest vacancy concentration of 1.0 ML for the (1×1)-$2O^1_{vac}$ structure using a $(4\times12\times1)$ *k* mesh, and the magnitude of the change was within ~3 meV/atom. Furthermore extending the $V_2O_5(001)$ slab from two to three layers (with the same vacuum thickness) revealed even smaller changes. The change in the calculated vacancy formation energy due to a larger plane-waves cutoff of 1200 eV was within ~0.3 meV/atom. These tests show that the errors induced by the standard numerical setup used are one order of magnitude smaller than differences between calculated $E_f^{(1/2)O_2}$ values at different vacancy concentrations and for different geometries.

The lowest vacancy formation energy is found for the (1×2)-$2O^1_{vac}$ ($\Theta=1/2$ ML) with vacancies sharing O^3 atoms forming rows along the [010] direction. The structures with vacancies sharing O^2 atoms are by 70 and 120 meV/atom less favorable than the corresponding structures in which vacancies share O^3 atoms at the 1/3 and 1/2 ML concentrations, respectively. In order to identify a possible reason for the preferred [010] direction, we first compare selected distances between vacancies for both geometries at both concentrations. The distance along the [100] direction between the [010] oriented pairs and rows equals the *a*-lattice parameter (11.55 Å). This renders any lateral interaction between the vacancies in neighboring pairs or rows rather unlikely. The closest distance between two vacancies along one row is approximately equal to the *b*-lattice parameter (3.58 Å). This distance increases by less than 0.05 Å only by decreasing the concentration up to 1/3 ML. Furthermore, the closest distance between neighboring vacancies sharing O^2 atoms is very similar to that between vacancies sharing O^3 atoms at both concentrations (3.52 Å), and distances along the [010] direction are large enough (~3*b* and ~2*b* at 1/3 and 1/2 ML, respectively) not to expect any sizable interaction. Thus, these structural considerations do not explain the preference for orienting along the [010] direction.

To this end, we have investigated the extent to which the gradualy increase in the defect concentration (from the isolated vacancy to the vacancy pairs and the missing rows) at the surface influences the resulting vacancy formation energy. Figure 6 shows the *nonaveraged* vacancy formation energy of each additional defect upon successive removal of oxygen along the row as calculated in a (1×3) geometry, and compares it to that resulting of the corresponding reduction along the [100] direction. Such values have been obtained by using the energy of the fully relaxed structures at the immediate lower concentration as the reference system. If vacancies sharing O^2 atoms are consecutively created, the removal of the second oxygen is by ~0.1 eV/atom larger than for the isolated defect. However, this analysis results in a completely different situation if vacancies sharing O^3 atoms are gradually created. The actual vacancy formation energy for each additional defect along the rows *decreases* with increasing defect concentration by about 50 meV/atom, thereby stabilizing the missing-row structure. This trend indicates that reduction may occur along the rows in a concerted way.

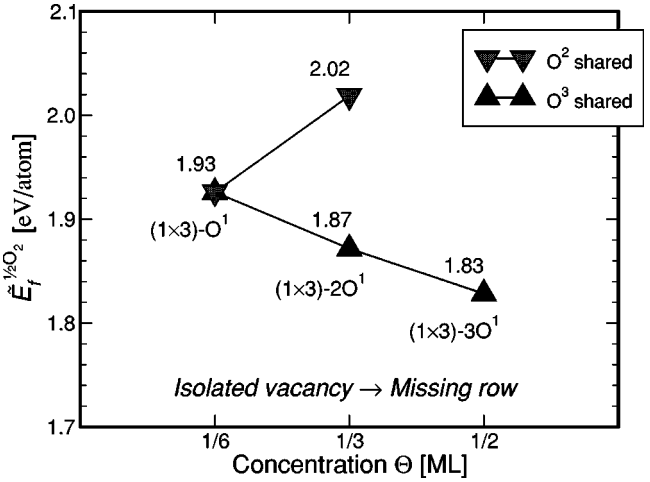

FIG. 6. Calculated *nonaveraged* vacancy formation energies $\tilde{E}_f^{(1/2)O_2}$ in eV/atom for each vacancy upon consecutive vacancy removal along both the [010] (O^3 shared) and [100] (O^2 shared) directions.

In Fig. 7 we show the energy profile upon successive vacancy formation that includes both unrelaxed and fully relaxed geometries. In all cases, the unrelaxed geometries corresponded to the fully relaxed structure at the immediate lower concentration with one additional vacancy being formed that was not allowed for further relaxation. We find that after the initial vacancy formation, it not only becomes *easier* to remove additional oxygen atoms along the rows of the unrelaxed structures, but the energy gained if structural relaxations are allowed remains approximately constant, leading to a reduced net formation energy for each subsequent vacancy. This correlates with the already described

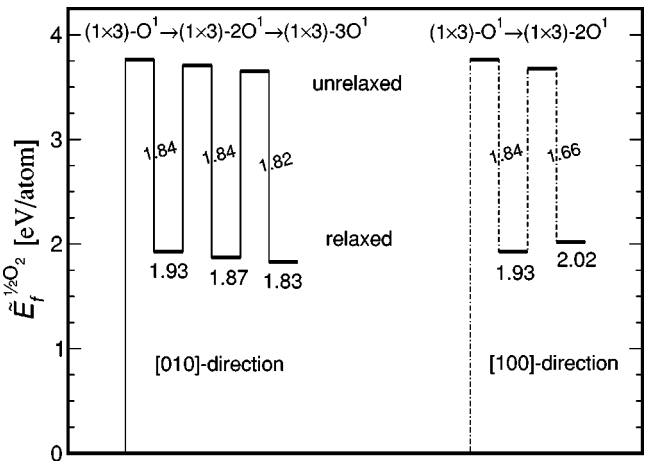

FIG. 7. Calculated *nonaveraged* vacancy formation energy sequence for each additional vacancy upon gradual removal of vacancies along both the [010] (O^3 shared, solid lines) and [100] (O^2 shared, dotted lines) directions. Shown are the relaxation contributions to the final values displayed in Fig. 6.

noncounteracting vacancy-induced relaxation effects with increasing coverage when vacancies orient themselves along the [010] direction (see Sec. III B). However, the relaxation contribution of 1.84 eV/atom at $\Theta=1/6$ ML is by about 0.2 eV larger than that for an additional vacancy forming a pair along the [100] direction. Thus, there is a correlation between the nonaveraged vacancy formation energy trend for both relevant alignments and the corresponding relaxations contributions to these energies. The counteracting lattice relaxation effects of vacancies sharing twofold coordinated oxygen atoms renders the reduction of the surface along this direction rather unlikely.

Additionally, we compute a higher vacancy formation energy at the higher 3/4 and 1.0 ML concentrations (cf. Table III). This, together with the preference for the missing-row structure at $\Theta=1/2$ ML, indicates that the reduction of the surface does *not* occur by random abstraction of vanadyl oxygen atoms at the surface. Consequently, we suggest that the trenches along the [010] direction at the $V_2O_5(001)$ surface provide preferred paths for continuous reduction of the surface at isolated defect sites that in turn may lead to a considerable concerted reduction of the surface.

To put the calculated formation energies into perspective, we compare them with corresponding values for the threefold and twofold coordinated surface oxygen atoms as well as that of bulk vanadyl oxygen atoms. The $V_2O_5(001)$ surface exposes five inequivalent oxygen atoms. Besides the four different oxygen sites indicated as O^1, O^2, O^3, and $O^{3'}$ in Fig. 1, an additional bridging oxygen, $O^{2'}$ that points outwards to the surface layer, also has to be considered. We calculated the vacancy formation energy for each inequivalent threefold and twofold surface oxygen atoms at a concentration of 1/4 ML and compare it with that for the terminal vanadyl oxygen at the same concentration. Table IV lists the results for both the unrelaxed and relaxed geometries.

We will not discuss in detail the structural relaxations induced by the two- and threefold coordinated vacancies, but mention that a single O^2, $O^{2'}$, O^3, or $O^{3'}$ vacancy does not introduce surface relaxations that lead to bond formation as the singly coordinated vanadyl oxygen does. For the latter, the relaxation contributions to the vacancy formation energy amount to 1.83 eV ($\Theta=1/4$ ML). The corresponding values for O^2 and $O^{2'}$ vacancies are smaller by ~0.4 eV, and for the O^3 and $O^{3'}$ vacancies by ~1.4 eV. Altogether, the ease of removal of the terminal vanadyl oxygen atoms is confirmed. For the removal of any of the other surface O atoms at least 1.67 eV more energy is required.

TABLE IV. Vacancy formation energy $E_f^{(1/2)O_2}$ in eV/atom for the unrelaxed and relaxed structures investigated at $\Theta=1/4$ ML.

Structure	Unrelaxed	Relaxed
(1×2)-O^1_{vac}	3.78	1.95
(1×2)-O^2_{vac}	5.09	3.68
(1×2)-$O^{2'}_{vac}$	5.09	3.62
(1×2)-O^3_{vac}	4.40	3.94
(1×3)-$O^{3'}_{vac}$	4.45	4.00

In bulk V_2O_5 the O-vanadyl vacancy formation is 1.97 eV/atom. The calculation was performed using a bulk supercell of 84 (83) atoms obtained by elimination of the vacuum in the (1×2) surface unit cell that contained three (001) oriented crystal layers. This is very similar to the 1.95 eV/atom for the formation of an isolated defect on the $V_2O_5(001)$ surface. This similarity and the existence of channels that are large enough to permit the diffusion of oxygen may relate to the observed facile (thermally and LEED beam induced) conversion of V_2O_5 into oxides such as V_6O_{13} and V_4O_9 once reduction has been initiated at the $V_2O_5(001)$ surface.[9,39] The structures of these lower oxides can be seen as (slightly distorted) superstructures of V_2O_5 resulting from bulk vanadyl oxygen loss.

The predicted energy of O-vacancy formation can be compared with estimates of the enthalpy of defect formation from conductivity measurements. The PW91 predictions of 1.97 to 1.95 eV are larger than the experimental estimates of 1.5 to 1.3 eV.[40] It is known that gradient corrected function-

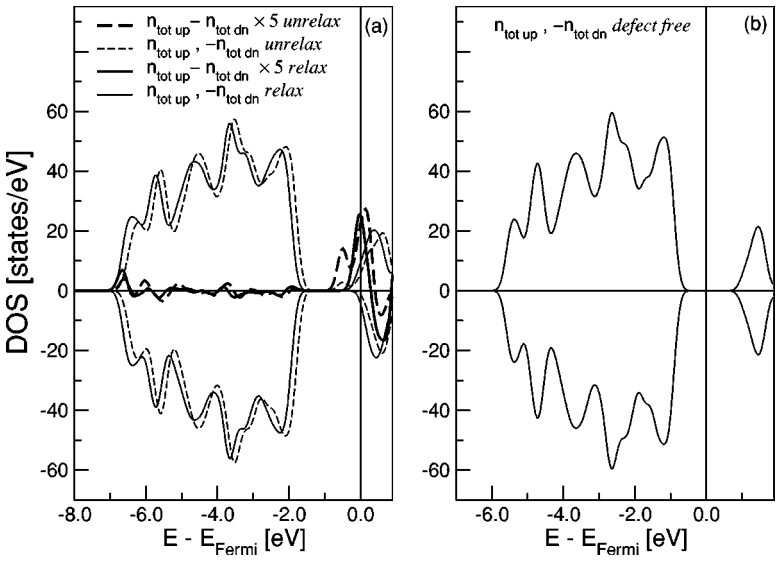

FIG. 8. Total spin-projected densities of states (DOS)(α-spin: $n_{tot\ up}$, β-spin: $-n_{tot\ dn}$,) of the (a) (1×3)-O^1_{vac} fully relaxed (solid thin lines) and unrelaxed (dashed thin lines) defect structure compared to the (b) defect-free $V_2O_5(001)$ surface. The curves are smoothed by a Gaussian level broadening of 0.2 eV. The thicker lines in (a) correspond to the difference between α- and β-spin states, and the values are multiplied by a factor of 5.

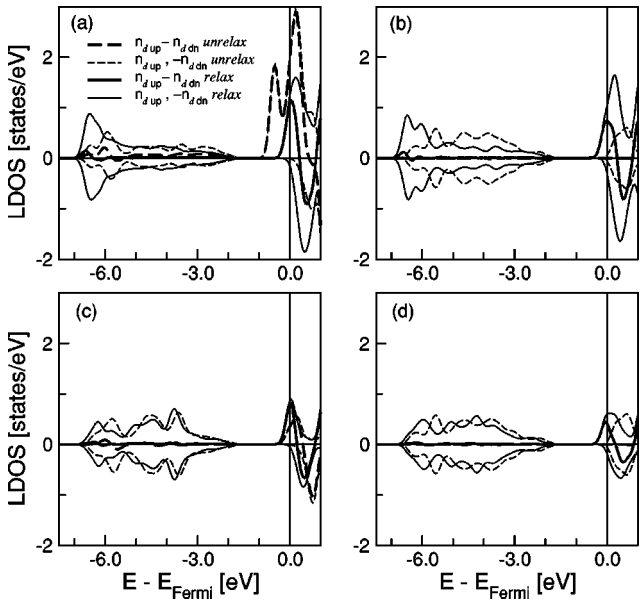

FIG. 9. Spin- and orbital projected densities of states (LDOS) (α-spin: $n_{d\ up}$, β-spin: $-n_{d\ dn}$,) of the (a) defect site, V_{vac} of the relaxed (1×3)-O^1_{vac} structure (solid thin lines) compared to the unrelaxed geometry (dashed thin lines) and (b), (c), and (d) correspond to the three V atoms labeled V_b, V_c, and V_d in Fig. 3(b), respectively. The curves are smoothed by a Gaussian level broadening of 0.2 eV. The thicker lines correspond to the difference between α- and β-spin states.

als such as PW91 (or PBE) tend to overestimate atomization energies of molecules[37] and adsorption energies of atoms and molecules on surfaces.[6] This overestimation has also been found for vanadyl bonds in small gas-phase species and on V_2O_5 surfaces.[41]

D. O-vacancy-induced electronic effects

V_2O_5 is an intrinsic semiconductor at room temperature with an optical band gap of 2.30–2.36 eV.[42,43] The lattice relaxation that occurs at the V_2O_5(001) surface upon reduction produces distinct changes in the surface electronic structure. Figure 8 compares the spin-projected total density of states of the isolated defect (1×3)-O^1_{vac} structure at 1/6 ML [Fig. 8(a)] with that of the defect-free surface [Fig. 8(b)]. Energies in Fig. 8 refer to the calculated Fermi level, which lies within the energy gap for an intrinsic semiconductor. Figure 8(a) also shows the difference DOS between up and down spin projections for the relaxed and unrelaxed geometries upon O removal. We observe virtually no contribution to the difference DOS from states within the valence band. The peak right at the Fermi level results from the partial occupation of the 3*d* orbitals on reduced V cations. Since a neutral oxygen atom is removed, *formally* two electrons are left at the vacancy site. The ground state of the reduced surface at 1/6 ML is a triplet. At all concentrations considered and for the different geometries, the highest spin state was found to be most stable.

Figure 9 shows the atom-, *d*-orbital-, and spin-projected densities of states (LDOS) at the O-vacancy defect site [Fig. 9(a)] and at the three other V atoms contained in a (010) oriented plane perpendicular to the V_2O_5(001) surface that intersects the defect site [Figs. 9(b)–9(d)]. The three V atoms are labeled V_b, V_c, and V_d in Fig. 3(b), respectively. The difference LDOS between both spin projections reveals that for the unrelaxed structure the two electrons occupy states of 3*d* character which are localized primarily on the defect site. Thus, if the structure did not strongly relax upon oxygen removal, the highest chemical reduction of V atoms (while reducing the vanadium coordination by 1) would be achieved. However, the structural relaxations result in a partial delocalization of the electrons over nearby metal sites, as clearly seen in Fig. 9. In other words, the electrons occupy *d* states which are partly localized on adjacent V cations and the degree of reduction at the defect site is smaller. Schematically,

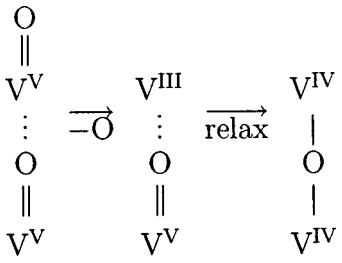

Note that the effect extends somewhat beyond the defect site and its counterpart at the second crystal layer [see Figs. 9(c) and 9(d)].

Turning to higher concentrations, we find similar effects at each vacancy site for all the structures investigated. These changes, together with the suggested continuous reduction of the V_2O_5(001) surface up to 1/2 ML, in which subsequent defects along the [010] direction are easier to form than the first isolated defect, provide a basis for suggesting a concerted reduction of the surface which involves not only the defect sites. However, this concerted surface reduction may decrease selectivity in catalytic applications.

IV. STABILITY OF REDUCED V_2O_5(001)

In the following, we will discuss briefly the stability of the reduced surface structures in thermodynamic equilibrium with an O_2 environment at finite temperatures. The thermodynamic formalism used to determine the most stable structures of the reduced V_2O_5(001) surface at a given temperature and O_2 partial pressure is described in detail in Refs. 44 and 45 and has been successfully applied in previous studies (see, for example, Refs. 46–48).

In the present study we are interested in the relative stability of the reduced surfaces $V_2O_5^{vac}$(001)

$$V_2O_5{}^{clean} \rightleftharpoons V_2O_5{}^{vac} + N_{vac}\frac{1}{2}O_2, \tag{3}$$

as a function of the vacancy concentration $\Theta = N_{vac}/N_{tot}$. We calculate the accompanying change of the surface-free energy $\Delta\gamma$ as

$$\Delta\gamma(T,p,\Theta) = \frac{1}{A}\left[G_{\mathrm{vac}}(T,p,N_{\mathrm{vac}}) - G_{\mathrm{clean}}(T,p) + N_{\mathrm{vac}}\frac{1}{2}\mu_{O_2}(T,p)\right]. \quad (4)$$

Here, $G_{\mathrm{vac}}(T,p,N_{\mathrm{vac}})$ and $G_{\mathrm{clean}}(T,p)$ are the Gibbs free energies of the supercells representing the reduced and the defect-free surfaces, respectively, and A is the area of the surface unit cell. In our calculations all surfaces are represented by periodically repeated slabs so that the Gibbs free energies refer to the content of one supercell. Both slabs contain the same number of V atoms, N_{V}, and N_{vac} is the number of O vacancies. The difference $\Delta\gamma$ is negative if the reduced surface is more stable than the clean surface, and positive otherwise.

The Gibbs free energies of the solid components in Eq. (4) are equated to the calculated DFT total energies that are evaluated at a certain volume of the unit cell, V and $T=0$ K. This means that contributions which depend on the vibrational modes in the system and those resulting from the pV term are neglected. As is apparent from Eq. (4), only the difference of Gibbs free energies enters the expression for $\Delta\gamma$. In Ref. 45 it was shown that the vibrational contributions to the entropy tend to cancel to a large extent, and that the influence of the pV term is even smaller. This allows us to rewrite Eq. (4) as

$$\Delta\gamma(T,p,\Theta) = \frac{1}{A}\left[E_{\mathrm{vac}}(\Theta) - E_{\mathrm{clean}} + N_{\mathrm{vac}}\frac{1}{2}\mu_{O_2}(T,p)\right]. \quad (5)$$

For a given chemical potential we predict which surface structure is the most stable by searching for the surface model with the lowest surface free energy.

It is important to consider bounds between which μ_{O_2} can vary. The V and O chemical potentials are not independent, because they are related to each other by the existence of the V_2O_5 bulk phase. Thus, a meaningful lower bound for $\frac{1}{2}\mu_{O_2}$ beyond which the oxide will decompose into V metal and oxygen is given by

$$\min\left[\frac{1}{2}\mu_{O_2}(T,p)\right] = \frac{1}{5}[G^{\mathrm{bulk}}_{V_2O_5} - 2G^{\mathrm{bulk}}_{\mathrm{V}}] = \frac{1}{5}[E^{\mathrm{bulk}}_{V_2O_5} - 2E_{\mathrm{V}}]. \quad (6)$$

Here, $G^{\mathrm{bulk}}_{V_2O_5}$ and $E^{\mathrm{bulk}}_{V_2O_5}$ are the Gibbs free energy and total energy of bulk V_2O_5 per bulk formula unit, and $G^{\mathrm{bulk}}_{\mathrm{V}}$ and $E^{\mathrm{bulk}}_{\mathrm{V}}$ the Gibbs free energy ($G^{\mathrm{bulk}}_{\mathrm{V}}=\mu_{\mathrm{V}}$) and total energy of metallic bcc vanadium.

A convenient upper bound for $\frac{1}{2}\mu_{O_2}$ is

$$\max\left[\frac{1}{2}\mu_{O_2}(T,p)\right] = \frac{1}{2}\mu_{O_2}(0\ \mathrm{K}) = \frac{1}{2}E_{O_2}, \quad (7)$$

where E_{O_2} is the total energy of a free, isolated molecule at $T=0$ K. Thus, the range of oxygen chemical potentials is

$$\frac{1}{5}[E^{\mathrm{bulk}}_{V_2O_5} - 2E^{\mathrm{bulk}}_{\mathrm{V}}] < \frac{1}{2}\mu_{O_2}(T,p) < \frac{1}{2}E_{O_2}. \quad (8)$$

Introducing the energy of formation $E_f^{V_2O_5}$ of the oxide

$$E_f^{V_2O_5} = \left[E^{\mathrm{bulk}}_{V_2O_5} - 2E^{\mathrm{bulk}}_{\mathrm{V}} - \frac{5}{2}E_{O_2}\right], \quad (9)$$

for which our DFT calculations give −16.41 eV (Ref. 49) (the experimental result for the heat of formation at 298 K is −16.07 eV, Ref. 50), Eq. (8) takes the form

$$\frac{1}{5}E_f^{V_2O_5} < \frac{1}{2}\mu_{O_2}(T,p) - \frac{1}{2}E_{O_2} < 0. \quad (10)$$

In the following we will use $\mu_{O_2}(0\ \mathrm{K})=E_{O_2}$ as a standard and give the chemical potential with respect to this standard as

$$\Delta\mu_{\mathrm{O}}(T,p) = \frac{1}{2}[\mu_{O_2}(T,p) - E_{O_2}]. \quad (11)$$

Inserting $\Delta\mu_{\mathrm{O}}$ into Eq. (5) and using Eq. (2), we obtain for the change of the surface energy $\Delta\gamma(T,p,\Theta)$

$$\Delta\gamma(T,p,\Theta) = \frac{N_{\mathrm{vac}}}{A}[E_f^{(1/2)O_2}(\Theta) + \Delta\mu_{\mathrm{O}}(T,p)]. \quad (12)$$

The chemical potential is then related to actual temperature and pressure conditions by assuming that the surface is in thermodynamic equilibrium with the gas phase. As the surrounding O_2 atmosphere forms an ideal gas reservoir, the expression

$$\mu_{O_2}(T,p) = [\mu_{O_2}(T,p^\circ) + RT\ ln(p/p^\circ)], \quad (13)$$

gives the pressure dependence of $\Delta\gamma(T,p,\Theta)$. p° is the pressure of a reference state ($p^0=1$ atm). The temperature dependence of the chemical potential $\mu_{O_2}(T,p^\circ)$ is given by

$$\mu_{O_2}(T,p^\circ) = \mu_{O_2}(0\ \mathrm{K}) + [H(T,p^\circ) - H(0\mathrm{K},p^\circ)] - T\,S(T,p^\circ). \quad (14)$$

Tabulated values for the enthalpy, H, and entropy, S, at the temperature T were used.[51]

In Fig. 10 we show the results of Eq. (12) for all the structures investigated. The chemical potential, $\Delta\mu_{\mathrm{O}}$, is translated into a pressure scale for $T=800$ K using Eqs. (11), (13), and (14) (see the upper axis in Fig. 10).

At the highest chemical potential so much oxygen is present in the gas phase that the stoichiometric $V_2O_5(001)$ surface is most stable. Towards lower chemical potentials (lower than 1.87 eV), the phase with defects forming a trench-like structure with a (1×1) periodicity at $\Theta=1/2$ ML becomes more stable. The other surfaces are higher in energy. The oxygen partial pressure ($\sim10^{-13}$ atm) corresponds to UHV conditions so that it is likely that the missing-row structure can be observed in experiment. Here, it is important to mention that the PW91 gradient approximation tendency to overestimate formation and binding energies means that the chemical potential might be shifted by several 100 meV. Thus, the absolute pressures might be wrong by 2 to 3 orders of magnitude. Nevertheless, the general stability trend is valid.

Furthermore, we calculate the value of the oxygen chemical potential below which bulk V_2O_5 would be reduced to VO_2

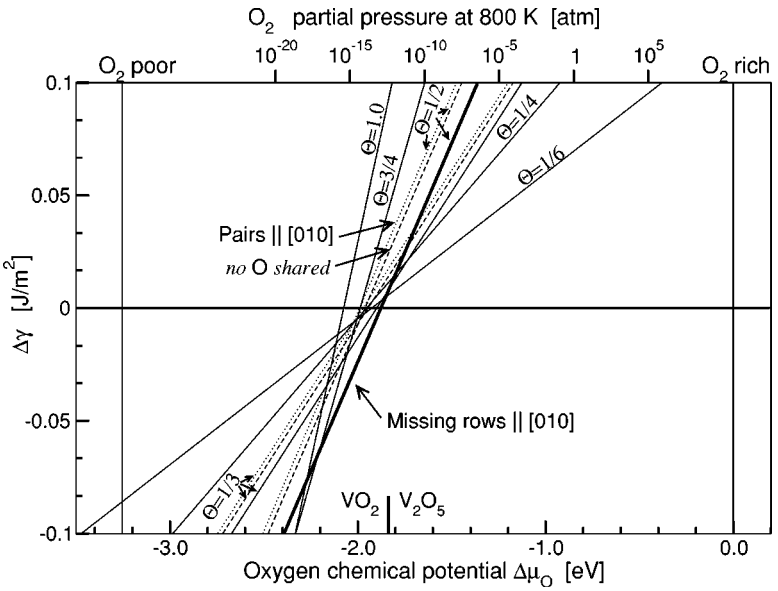

FIG. 10. Surface energy change $\Delta\gamma(T,p,\Theta)$ as a function of the chemical potential $\Delta\mu_O$ for different vacancy concentrations Θ. In the top x axis, the chemical potential $\Delta\mu_O(T,p)$ has been translated into a pressure scale at $T=800$ K. The vertical lines indicate the allowed range of $\Delta\mu_O$. The three different configurations at $\Theta=1/3$ with vacancies sharing either O^3, O^2 or not sharing O atoms are shown as full, dashed, and dotted lines, respectively. For the corresponding geometries at $1/2$ ML the same type of lines are used. However, for the most stable structure at $1/2$ ML with vacancies sharing O^3 atoms a thicker, full line is used.

$$V_2O_5 \rightleftharpoons 2VO_2 + \tfrac{1}{2}O_2.$$

The V and O chemical potentials are once more not independent, i.e.,

$$\frac{5}{2}\mu_{O_2} + 2\mu_V = G^{\text{bulk}}_{V_2O_5} = E^{\text{bulk}}_{V_2O_5},$$

$$\frac{4}{2}\mu_{O_2} + 2\mu_V = 2\ G^{\text{bulk}}_{VO_2} = 2\ E^{\text{bulk}}_{VO_2},$$

and the condition for the oxygen chemical potential at which the lower bulk oxide is thermodynamically more stable is expressed as

$$\frac{1}{2}\mu_{O_2} < E^{\text{bulk}}_{V_2O_5} - 2E^{\text{bulk}}_{VO_2}. \tag{15}$$

Here, $E^{\text{bulk}}_{VO_2}$ is the total energy of bulk VO_2 in the rutile structure per bulk formula unit.[52] Introducing the energy of formation of both oxides into Eq. (15) and using Eq. (11) leads to

$$\Delta\mu_O < E_f^{V_2O_5} - 2E_f^{VO_2}. \tag{16}$$

The calculated $E_f^{VO_2}=-7.29$ eV (Ref. 53) compares well with the experimental heat of formation of β-VO_2 at 298 K $H_f^{VO_2}=-7.33$ eV.[54] We obtain $\Delta\mu_O=-1.84$ eV for this bound (see Fig. 10). This implies an oxygen partial pressure of about 4×10^{-13} atm at 800 K, and a temperature of about 1600 K at standard pressure. Inspection of the V-O bulk phase diagram[54] indicates that at standard pressure and moderate temperatures V_2O_5 is thermodynamically more stable than lower oxides. The latter are stable at higher temperatures and low oxygen pressures, e.g., ~800 K and UHV conditions. Furthermore, the chemical potential at which the missing-row structure is likely to be observed corresponds also to strongly reducing conditions. As mentioned above, at 800 K a partial pressure of approximately 10^{-13} atm corresponds to $\Delta\mu_O\approx-1.87$ eV, which is not significantly different from the value of −1.84 eV ($p\sim4\times10^{-13}$ atm) for the decomposition of V_2O_5 into $2VO_2+\frac{1}{2}O_2$. Thus, the reduction that starts at the surface may initiate the conversion to the lower bulk oxide.

V. SUMMARY

The vanadyl oxygen vacancy formation energy at the V_2O_5(001) surface has been studied for nonrandom vacancy structures as a function of vacancy concentration, Θ. We find a large inward relaxation of the surface layer at the defect sites at all concentrations investigated. In addition, corresponding V atoms at the second substrate layer relax in the opposite direction so that bonds between the layers are formed. The distinct possibility of V_2O_5(001) of forming bonds between the crystal layers reduces the cost of oxygen removal significantly.

The calculations suggest that the surface reduction might take place cooperatively and that a missing-row structure with a (1×1) periodicity forms at $\Theta=1/2$ ML. The ease of reduction along the [010] direction with vacancies sharing threefold coordinated oxygen atoms has been explained as a concerted lattice relaxation effect induced by subsequent removal of vanadyl O atoms along the [010] oriented trenches. Under reducing conditions (low oxygen partial pressure and $T=800$ K) the missing-row structure is more stable than the defect-free surface. Furthermore, the vacancy-induced relax-

ations were found to have a distinct effect on the electronic structure of the reduced surface. The defect V sites are not reduced to V^{III} upon O removal due to charge delocalization onto neighboring V atoms. Preventing the strong relaxations observed for crystalline V_2O_5 upon surface reduction by, e.g., isolating the defect site from the V_2O_5 layer beneath, will increase the vacancy formation energy. A way to do so is to *anchor* the defect site onto a support. Hence, if oxygen removal is the crucial catalytic step, site isolation in supported vanadia will reduce the activity, but may increase selectivity. Thus, understanding the role of the support is a clear priority in the design of vanadium oxide based catalysts. Therefore, our current research is directed towards modeling supported vanadium oxide catalysts, and we have found that oxygen removal is indeed much more difficult from V_2O_5 layers supported on α-$Al_2O_3(0001)$ than from the single crystal $V_2O_5(001)$ surface.[29]

ACKNOWLEDGMENTS

This work has been supported by the Deutsche Forschungsgemeinschaft (SFB 546) and the Fonds der Chemischen Industrie. We would like to thank G. Kresse and A. Eichler for helpful comments on the VASP code. We are grateful to V. Brázdová, A. Hofmann, J. Döbler, and A. Seitsonen for useful discussions. The calculations were carried out at both the Cray T3E computer of the Konrad-Zuse-Zentrum für Informationstechnik in Berlin (ZIB) and the IBM p690 system of the Nordeutscher Verbund für Hoch- und Höchstleistungsrechnen (HLRN). We thank B. Kallies from ZIB for technical support.

*Corresponding author: vgp@chemie.hu-berlin.de

[1] B. M. Weckhuysen and D. E. Keller, Catal. Today **78**, 25 (2003), and references therein.
[2] P. Mars and D. W. van Krevelen, Spec. Suppl. Chem. Eng. Sci. **3**, 41 (1954).
[3] R. Enjalbert and J. Galy, Acta Crystallogr., Sect. C: Cryst. Struct. Commun. **42**, 1467 (1986).
[4] W. Lambrecht, B. Djafari-Rouhani, and J. Vennik, Solid State Commun. **39**, 257 (1981).
[5] W. Lambrecht, B. Djafari-Rouhani, and J. Vennik, Surf. Sci. **126**, 558 (1983).
[6] B. Hammer, L. B. Hansen, and J. K. Nørskov, Phys. Rev. B **59**, 7413 (1999).
[7] K. Hermann, M. Witko, R. Druzinić, and R. Tokarz, Appl. Phys. A: Mater. Sci. Process. **A72**, 429 (2001).
[8] Z. Zhang and V. E. Henrich, Surf. Sci. **321**, 133 (1994).
[9] M. N. Colpaert, P. Clauws, L. Fiermans, and J. Vennik, Surf. Sci. **36**, 513 (1973).
[10] L. Fiermans and J. Vennik, Surf. Sci. **18**, 317 (1969).
[11] L. Fiermans and J. Vennik, Surf. Sci. **9**, 187 (1968).
[12] R. L. Smith, W. Lu, and G. S. Rohrer, Surf. Sci. **322**, 293 (1995).
[13] P. Hohenberg and W. Kohn, Phys. Rev. **136**, B864 (1964).
[14] W. Kohn and L. J. Sham, Phys. Rev. **140**, A1133 (1965).
[15] M. C. Payne, M. P. Teter, D. C. Allan, T. A. Arias, and J. D. Joannopoulos, Rev. Mod. Phys. **64**, 1045 (1992).
[16] G. Kresse and J. Hafner, Phys. Rev. B **48**, 13115 (1993).
[17] G. Kresse and J. Furthmüller, Comput. Mater. Sci. **6**, 15 (1996).
[18] G. Kresse and J. Furthmüller, Phys. Rev. B **54**, 11169 (1996).
[19] The version VASP4.4.5 released on 26 November 2001 has been used.
[20] J. P. Perdew, J. A. Chevary, S. H. Vosko, K. A. Jackson, M. R. Pederson, D. J. Singh, and C. Fiolhais, Phys. Rev. B **46**, 6671 (1992).
[21] J. P. Perdew, J. A. Chevary, S. H. Vosko, K. A. Jackson, M. R. Pederson, D. J. Singh, and C. Fiolhais, Phys. Rev. B **48**, 4978(E) (1993).
[22] P. E. Blöchl, Phys. Rev. B **50**, 17953 (1994).
[23] G. Kresse and D. Joubert, Phys. Rev. B **59**, 1758 (1999).
[24] H. J. Monkhorst and J. D. Pack, Phys. Rev. B **13**, 5188 (1976).
[25] F. D. Murnaghan, Proc. Natl. Acad. Sci. U.S.A. **30**, 244 (1944).
[26] X. Yin, A. Fahmi, A. Endou, R. Misura, I. Gunji, R. Yamauchi, M. Kubo, A. Chatterjee, and A. Miyamoto, Appl. Surf. Sci. **130–132**, 539 (1998).
[27] J. S. Braithwaite, C. R. A. Catlow, J. D. Gale, and J. H. Harding, Chem. Mater. **11**, 1990 (1999).
[28] G. Kresse, S. Surnev, M. G. Ramsey, and F. P. Netzer, Surf. Sci. **492**, 329 (2001).
[29] V. Brázdová, M. V. Ganduglia-Pirovano, and J. Sauer, Phys. Rev. B **69**, 165420 (2004).
[30] A. Chakrabarti, K. Hermann, R. Druzinic, M. Witko, F. Wagner, and M. Petersen, Phys. Rev. B **59**, 10583 (1999).
[31] S. Tsuzuki, K. W. Jacobsen, and J. K. Nørskov, J. Chem. Phys. **114**, 3949 (2001).
[32] H. Rydberg, M. Dion, N. Jacobson, E. Schröder, P. Hyldgaard, S. I. Simak, D. C. Langreth, and B. I. Lundqvist, Phys. Rev. Lett. **91**, 126402 (2003).
[33] M. V. Bollinger, K. W. Jacobsen, and J. K. Nørskov, Phys. Rev. B **67**, 085410 (2003).
[34] H. Rydberg, N. Jacobson, P. Hyldgaard, S. I. Simak, B. I. Lundqvist, and D. C. Langreth, Surf. Sci. **532**, 606 (2003).
[35] W. Theis (Free University Berlin), personal communication (2004).
[36] G. Herzberg, *Molecular Spectra and Molecular Structure. I. Spectra of Diatomic Molecules*, 2nd ed. (Krieger, Malabar, FL, 1989).
[37] J. P. Perdew, K. Burke, and M. Ernzerhof, Phys. Rev. Lett. **77**, 3865 (1996).
[38] Y. Zhang and W. Yang, Phys. Rev. Lett. **80**, 890 (1998).
[39] L. Fiermans, P. Clauws, W. Lambrecht, L. Vandenbroucke, and J. Vennik, Phys. Status Solidi A **59**, 485 (1980).
[40] P. Kofstad, *Nonstoichiometry, Diffusion, and Electrical Conductivity in Binary Metal Oxides* (Wiley, New York, 1972).
[41] J. Sauer and J. Döbler, J. Chem. Soc. Dalton Trans. (to be published).
[42] N. Kenny, C. R. Kannerwurf, and D. H. Whitmore, J. Phys. Chem. Solids **27**, 1237 (1966).
[43] Z. Bodó and I. Hevesi, Phys. Status Solidi **20**, K45 (1967).
[44] M. W. Finnis, Phys. Status Solidi A **166**, 397 (1998).

[45] K. Reuter and M. Scheffler, Phys. Rev. B **65**, 035406 (2001).
[46] O. Dulub, U. Diebold, and G. Kresse, Phys. Rev. Lett. **90**, 016102 (2003).
[47] J. Padilla and D. Vanderbilt, Phys. Rev. B **56**, 1625 (1997).
[48] B. Meyer, Phys. Rev. B **69**, 045416 (2004).
[49] The calculated total energies for bulk V_2O_5, bulk V, and O_2 are −58.755 841, −8.927 977, and −9.794 352 eV/formula unit.
[50] *NIST Chemistry WebBook*, edited by P. J. Linstron and W. G. Mallard (National Institute of Standards and Technology, Gaithersburg, MD, 2001); (http://webbook.nist.gov).
[51] *CRC Handbook of Chemistry and Physics*, 76th ed., edited by D. R. Lide and H. P. Frederiske (CRC Press, Boca Raton, FL, 1995).
[52] The optimized lattice parameters are $a=4.590$ Å and $c=2.844$ Å, and the corresponding experimental values 4.55 and 2.85 Å, respectively (Ref. 55). For this spin-polarized calculation we used a $(10\times10\times12)$-k mesh and other parameters as in Sec. II.
[53] The calculated total energy for bulk VO_2 is −58.755 841 eV/formula unit.
[54] W. Brückner, H. Oppermann, W. Reichelt, J. I. Terukow, F. A. Tschudnowski, and E. Wolf, *Vanadiumoxide Darstellung, Eigenschaften, Anwendung* (Akademie, Berlin, 1983).
[55] D. Taylor, Br. Ceram. Trans. J. **83**, 32 (1984).
[56] For $\Theta=1/6$ ML the calculated total energies are $E_{\mathrm{vac}}(\Theta)=-697.628\ 936$ eV and $E_{\mathrm{clean}}=-704.452\ 188$ eV.